Functional and morphological alterations of the light perception circuits in postmortem retina from donors at different stages of Alzheimer's disease

Nicolae Sanda (1)(2), Dan Milea (3)(4), Eniko Kovari (5), Yixin Tong (6)(7), Talayeh Brügger (8), Jens Hannibal (9), Kristof Levente Egervari (10), Johannes Alexander Lobrinus (10), Emmanuel Carrera (2)(11), Gabriele Thumann (2)(12), Sonja Kleinlogel (8)(13), Antoine Adamantidis (7)(14), Ludovic S. Mure (6)(7)(14)*

Affiliations

(1) Fribourg Cantonal Hospital, Neurology Department, Fribourg, Switzerland

(2) Department of Clinical Neurosciences, Geneva University, Geneva, Switzerland

(3) Rothschild Foundation Hospital, Neuro-ophthalmology Department, Paris, France

(4) Singapore National Eye Centre, Singapore and Duke-NUS Medical School, Singapore

(5) Faculty of medicine, University of Geneva, Switzerland

(6) Inselspital, Department of Ophthalmology, Bern, Switzerland

(7) University of Bern, DBMR, Bern, Switzerland

(8) University of Bern, Institute of Physiology, Bern, Switzerland

(9) Department of Clinical Biochemistry, Bispebjerg Hospital, Department of Clinical Medicine, Faculty of Health and Medical Sciences, University of Copenhagen, Copenhagen, Denmark

(10) Geneva University Hospital, Neuropathology Unit, Geneva, Switzerland

(11) Geneva University Hospital, Stroke Center, Geneva, Switzerland

(12) Geneva University Hospital, Ophthalmology Department, Geneva, Switzerland

(13) current address: F. Hoffmann-La Roche Ltd, Translational Medicine Neuroscience, Basel, Switzerland

(14) Inselspital, Zentrum für Experimentelle Neurologie, Department of Neurology, Bern, Switzerland.

*correspondence: ludovic.mure@unibe.ch

Abstract

Disruption of sleep and circadian rhythms is one of the earliest symptoms of Alzheimer's disease (AD). Circadian entrainment and modulation of alertness are non-visual responses to light driven by intrinsically photosensitive retinal ganglion cells (ipRGCs).

To explore structural and functional changes of ipRGCs and ipRGC circuits in AD, we analyzed the retinas and brains of 13 elderly patients ranging from normal cognition to AD and performed *ex vivo* extracellular electrophysiological recordings on freshly harvested retinas.

While rods and cones were moderately impaired, there was a severe loss of ipRGCs in AD donors. Importantly, the remaining ipRGCs exhibited morphological alterations, hyperexcitability, and were not able to sustain high levels of activation. These changes may be ipRGC subtype-specific and correlated with disease progression.

Altered ipRGC circuits and function could contribute to the disruption of sleep and circadian rhythms reported in AD patients. Measuring ipRGC-dependent responses to light could be a promising way to predict or monitor pathological changes in the brain.

Introduction

Alzheimer's disease (AD) is a devastating neurodegenerative disorder and the most common cause of dementia. characterized by progressive cognitive decline, memory loss, and impaired daily functioning[1]. AD neuropathological features, such as the presence of amyloid-beta plaques and tau protein-containing tangles, play a central role in disease progression. A definitive and unambiguous diagnosis is difficult to establish, and by the time it is obtained, the disease has usually progressed over decades, causing significant neurodegeneration. It is estimated that dementia affects more than 55 million patients, however its prevalence continues to rise as the population ages, and it is projected to double by 2050[2]. Understanding the underlying disease mechanisms and identifying potential early biomarkers is urgently needed to allow timely diagnosis and intervention.

One of the earliest symptoms in AD is a disruption of sleep and circadian rhythms. Individuals with Alzheimer's often experience increasingly fragmented sleep and an altered core body temperature rhythm[3–6]. There is now abundant evidence that disruption of the daily rhythms can occur years before the emergence of classical symptoms, such as memory loss in AD[7,8]. Excessive daytime sleepiness and sleep behavior disorders are associated with an increased risk of developing AD and dementia suggesting that dysregulation of sleep may be important in the early pathogenesis of neurodegeneration[9–12]. These behavioral disruptions compromise not only the quality of life of the patient, but they also cause physical and psychological fatigue in the caregiver, often resulting in institutional placement.

The regulation of non-visual responses to light, including the synchronization of the circadian clock to the day-night cycle, as well as the regulation of sleep, alertness, mood and the pupillary light reflex (PLR), is primarily mediated by a class of intrinsically photosensitive retinal

ganglion cells (ipRGCs) that express the light-sensing protein melanopsin. Accordingly, when ipRGCs are selectively ablated or when signaling properties of melanopsin are changed, photoentrainment of the clock, acute light-modulation of sleep, and PLR to light are abolished or maladapted[13–16]. Interestingly, a recent histological study has shown a specific decline in the number of ipRGCs in the retina of AD patients[17]. Beta amyloid accumulation was also observed inside and around ipRGCs suggesting that the response properties of ipRGCs from AD patients may be altered[17]. In mouse models of AD, ipRGC anomalies have also been reported[18,19]. While these observations suggest that light perception circuits may be damaged in Alzheimer's disease, this has never been investigated further in patients.

The aim of this study was to evaluate the alteration of light perception in AD patients compared to normal individuals, using a comprehensive exploration in eye-brain donors. Specifically, we examined the histological and functional changes in ipRGC circuits in the retina and brain of individuals at different stages of Alzheimer's disease. We found that ipRGC-mediated photoreception was severely altered in AD; a fraction of ipRGCs underwent degeneration, while the remaining cells exhibited morphological alterations, hyperexcitability, and an inability to sustain high levels of activation. These changes may have been subtype-specific and correlated with disease progression. Although our findings are limited by the small size of our sample, they emphasize the importance of further investigating ipRGCs in order to manage symptoms associated with ipRGC-mediated responses to light, to develop diagnostic tools, to design novel therapeutic strategies and, more generally, to unravel early the pathophysiological mechanisms leading to neuronal degeneration in AD.

97 **Results**

98 To assess the impact of AD on light perception, we conducted an exploratory, multi-angle
99 study on 13 eye and brain donors, deceased at the Geneva Stroke Center (Geneva, Switzerland,
100 **FigS1A**). The demographic characteristics of the cohort are presented in **Table 1**. Ages ranged
101 from 69 to 103 years (81.31 ± 3.011). There were 9 males (mean age 79.44 ± 3.17 years; 69 to 97
102 years) and 4 females (mean age 85.50 ± 7.01 years; 70 to 103 years, p=0.49, Mann Whitney test).
103 The cause of death was brain infarct and/or brain hemorrhage (**Table1**). Among the included
104 donors, two showed ante-mortem signs of dementia (donors 3 and 5), which, together with their
105 post-mortem neuropathology, support a diagnosis of Alzheimer's disease and are therefore referred
106 to in this manuscript as AD donors, as opposed to donors without known cognitive impairments
107 (ND, non-demented, donors). The neuropathological severity of tau lesions and amyloid
108 deposition were assessed in the anterior hippocampus, entorhinal, transentorhinal, and inferior
109 temporal cortices using the Braak staging for neurofibrillary tangles (NFT) and the Thal phases
110 for senile plaques (SP) (**FigS1B-D)**[20,21]. Thal phases ranged from 0 to 4 and Braak scores ranged
111 from I to VI. The two AD patients scored 3 and 4 and V and VI respectively **(Table1**). While Thal
112 phases were correlated with the age of the donors, Braak stages were not (**FigS1E**).

113 To quantify AD hallmarks along some of the brain circuits implicated in the regulation of
114 visual and non-visual responses to light, we also examined tau pathology and amyloid deposition
115 in 13 brain regions implicated in vision (LGN, SC, visual cortex), circadian rhythms (SCN),
116 alertness and sleep regulation (POA, pons nuclei), mood (AMY, LHB/pLHB, ACC), and pupillary
117 reflex to light (EWN) in 13 donors (**Fig1A**). Uniform brain sampling was performed by a
118 neuropathologist and SP and NFT were scored on a 0 to 3 scale by trained pathologists (0=none,
119 1=sparse, 2=moderate, 3=abundant) (**Fig1B**). We found aggregates in most of the regions

120 examined. While deposits of Amyloid beta (Aβ) were more abundant as the amyloid pathology
121 progresses, hyperphosphorylated tau (p-tau) burden did not follow this pattern and its presence in
122 light perception circuits appeared uncorrelated with Braak stages (**Fig1C, FigS2A**). Aβ burden in
123 the VC and Acc as well as in all retino-recipient nuclei except the LGN correlated with the Thal
124 phase of the respective donor (**Fig1C**).

125 To evaluate the correlation between the brain and retina pathologies, we performed
126 immunostaining of Aβ and Tau in the retina of the donors. We manually segmented the outer retina
127 (OR: photoreceptor (PR) and outer plexiform layers (OPL)) and inner retina (IR: inner nuclear
128 (INL), inner plexiform (IPL), and retinal ganglion cell (RGC) layers) (**Fig1D**) and determined the
129 layer distribution of p-tau and Aβ burdens in retinal cross sections. Representative microscopic
130 images show an accumulation of p-tau in patients that correlates with the Braak stage (**Fig1E**).
131 Immunostaining of p-tau revealed diffuse staining in the OPL and intense staining in the INL and
132 IPL, including probable intracellular staining in the INL. Aβ deposits were identified in the inner
133 retina, in particular in the innermost RGC and retinal nerve fiber layers. Aβ42 burden (**Fig1E,**
134 **FigS2B**) also increases with the Thal phase of the donor. Finally, we also measured the thickness
135 of the segmented IR and OR as a proxy of neurodegeneration. The thickness of IR layer decreased
136 with AD and was negatively correlated with the increase of Thal phases and Braak stages (**Fig1F,**
137 **FigS2C**).

138 The presence in the retina of both Aβ and Tau aggregates and degeneration (**Fig1**)
139 suggested a possible alteration of the light information sent to the brain. To evaluate the function
140 of the rods, cones, and ipRGCs, we recorded responses to light from a donor's retina preparation
141 using multi-electrode array (MEA)[22,23]. Briefly, the eyes of the donors were collected within 2
142 hours postmortem (**Table1**), immediately preserved in oxygenated Ames 'medium placed in a

143 light-proof container, transported to the lab where circular (3mm diameter) patches of retina were
144 dissected under dim red light, placed on MEA, and allowed to recover in darkness for at least 1
145 hour.

146 First, to evaluate photoreceptor function, we recorded micro-electroretinograms
147 (mERGs)[24] on retinal patches from five donors (**Table1**), including the two AD donors in response
148 to sequences of 10ms light flashes of increasing irradiance (470nm, 6.10^9 to 2.10^{13} photons/cm^2/s)
149 (**FigS3**)**.** mERG did not display major differences in response profiles between AD and age-
150 matched control donors (**FigS3A**). A-waves were detected in all donors at all light irradiances used
151 while b-waves were only clearly detected at the highest light stimulation but in all donors too[23].
152 While the amplitude of the a-wave from the AD donors was the smallest, it was not different from
153 that of the other donors. Similarly, the b wave amplitude and the latencies of both waves did not
154 differ between donors (**FigS3B, C**).

155 Then, to evaluate ipRGCs' function, we performed extracellular electrophysiological
156 recordings of freshly harvested retina from 6 donors including the two AD donors (**Table 1**). For
157 this purpose, the recording medium was supplemented with synaptic blockers to block rod and
158 cone input to RGCs and capture ipRGCs intrinsic, melanopsin-initiated signal. In response to 30s
159 pulses of monochromatic blue light (470 nm), photoresponsive cells were found in retinas from
160 each of the six donors (**Fig2A**). However, the number of ipRGCs varied from one donor to the
161 other. For each retina sample, we identified photoresponsive cells at an average density ranging
162 from <1 to ~8 cells/mm^2 (**Fig2B**). The number of light responsive cells was negatively correlated
163 with the Braak stage but not with the Thal phase, the age of the donor, or the delay of collection
164 of the eye (**Fig2B and FigS4A**). Grouped analysis reveals a two-fold decrease in ipRGCs density
165 in retina pieces from AD donors (**FigS4B**).

166 To confirm the ipRGC loss in AD patients, we performed immunostaining against
167 melanopsin as previously described[25] and we counted melanopsin-positive (mel+) cells in 3 mm
168 diameter retinal patches (**Fig2C**). We found about two times decreased density of mel+ in the
169 retina of AD donors (**FigS4B**). When examined individually, mel+ density correlated with the
170 patient Braak stage and ipRGCs density, but not with the Thal phase (**Fig2D, E and FigS4C**).
171 Melanopsin staining revealed that not only the number, but also the morphology of mel+ cells is
172 affected by the disease. In each retina sample, a blinded investigator used semi-automated tracing
173 to reconstruct the dendritic arborization of 4 mel+ cells per retina sample (**Fig2F**). Scholl analysis
174 revealed that while the extend radius of the ipRGCs dendritic tree was not different between
175 donors, its number of intersections midway between the soma and the extremities was decreased
176 in AD donors (**Fig2G, FigS4D**). Accordingly, both number of nodes and terminal branches were
177 lower in the AD patients (**Fig2H-I, FigS4D**). These results suggest a decrease in dendritic tree
178 complexity in AD. Interestingly, AD ipRGCs had larger soma (**Fig2J, FigS4D**). Altogether, these
179 major morphological alterations strongly suggest that the function of the surviving ipRGCs is also
180 altered.

181 To evaluate potential functional alterations in the remaining ipRGCs from AD donors, we
182 characterized their response properties. We stimulated the retinas for 30 s at increasing irradiances
183 of monochromatic blue light (470 nm, 2.10^{12} to 1.10^{15} photons/cm^2/s). Overall, responses to light
184 were slow, sustained, and outlasted the stimulus by several seconds after the light was switched
185 off, the sensitivity was low as previously described[22] (**Fig2A**). Response properties followed
186 similar dynamics with increasing stimulation irradiance; latency decreased while the duration and
187 number of spikes of the response increased (**Fig3A**). Interestingly, responses from donors at more
188 advanced stages of the disease appeared stronger at lower light intensities reflecting an increased

189 sensitivity or excitability with the progression of the disease (**Fig3B,C**). Conversely, in these
190 donors, responses to the highest intensity of light were diminished or even sometimes abolished,
191 suggesting a failure to sustain responses at advanced stages of AD (**Fig3B,C**).

192 Several morphological and functional ipRGC subtypes have been described in the human
193 retina[22,25–28]. To assess whether the alterations reported above reflect alteration and/or
194 degeneration of specific subtype(s), we performed principal components analysis (PCA) on the
195 response parameters of each ipRGCs recorded. Data separated into at least three main clusters
196 (**Fig3D**) whose response to light properties and time course closely resemble those from previously
197 described ipRGC subtypes[22] (**Fig3C,D,**). The three subtypes were found in all donors, but their
198 distribution was changed in the AD donors. Type 1 accounted for half of the ipRGCs in AD donors
199 while type 2 and 3 ipRGCs fraction was strongly decreased (**Fig3E**). When examined individually,
200 type 1 fraction correlates with the Braak stage of the donor (**FigS4E**). This result suggests that type
201 1 cells may be more resilient than type 2 and 3. As type 1 ipRGCs are the subtype that is most
202 sensitive to light, the increased excitability observed could be due to this change of distribution.
203 To test this hypothesis, we examined the sensitivity to light of each subtype. We found that type 1
204 ipRGC sensitivity was increased in AD donors (**Fig3F**). Overall, all ipRGC subtypes are affected
205 and the increased excitability observed in AD may rely on both a shift in subtypes distribution
206 toward type 1, the most sensitive ipRGCs, and an increase in their sensitivity.

207

208 **Discussion**

209 In this prospective study, we examined several circuits of light perception in a cohort of
210 elderly adult donors at various stages of AD pathological changes. Using a comprehensive suite
211 of measurements, we provide the first picture of how AD may impact ipRGCs abundance,

212 function, and brain targets. We found that the light signals conveyed by ipRGCs to the brain are
213 largely altered with AD, both quantitatively and qualitatively. These changes seem to correlate
214 with the progression of the disease and may affect subtypes selectively. Importantly, we highlight
215 the potential of ipRGCs as both biomarkers for AD and models to study the mechanisms of
216 neuronal degeneration in humans.

217 In the retina, our results are in agreement with the presence and distribution of AD
218 hallmarks and their correlation with the neuropathological changes observed in the brain, reported
219 early and in extensive postmortem retinal histological studies ([29–33](for review see[34])). We also
220 confirmed the loss of ipRGCs observed in AD patients[17]. We extended these findings by measuring
221 *ex vivo* the function of the different photoreceptors. Both outer and inner retina photoreceptors
222 seem to malfunction with AD but, while rods/cones response alteration may be limited to small
223 decreases in amplitude at specific light intensity levels, ipRGCs injury is massive.

224 AD has been associated with various forms of visual dysfunction, including abnormal
225 visual fields, reduced color and contrast vision which can be, at least in part, attributed to retinal
226 and optic nerve damage[35–38]. Retinal abnormalities can be identified with electroretinogram (ERG)
227 in AD [39–43]. Here, while we found a decrease in IR thickness, the mERG a and b waves did not
228 show significant differences between AD and ND patients in response to our stimulation protocol.
229 Because IR photoreceptor function declines rapidly with hypoxia[23], some differences between
230 donors may have been masked by the postmortem functional decline in all donors.

231 ipRGCs are the main contributors and in some cases the exclusive conduits of light
232 regulation to non-visual light responses[13,14]. Accordingly, they project to more than a dozen of
233 brain regions implicated in visual and non-visual responses to light, including the nuclei
234 investigated here: SCN, POA, HB/pHb, AMY, LGN, and SC[44,45]. We found twice less ipRGCs in

235 AD donors, and the surviving ones displayed abnormal morphologies and responses to light that
236 may precede degeneration. In particular, the increase in soma size resembles the phenomenon
237 called neuronal ballooning that is thought to result from deficient axonal trafficking and
238 subsequent accumulation of cargos at the initial segment[46–48]. Then, the increased excitability is
239 reminiscent of cerebral neurons in which an increased excitability is observable at the earlier stages
240 of the disease before there is pronounced cell loss and hypoactivity[49–51]. The initial loss of ipRGCs
241 may be biased toward types 2 and 3, with type 1 ipRGC appearing more resilient. Of note, while
242 the response profiles of ipRGC subtypes in AD donors seem to remain similar to their counterparts
243 from control donors (**Fig3C**), this result would need confirmation as the properties on which the
244 classification is based are altered and thus could lead to misclassification. M1 ipRGCs, the
245 morphological equivalent of functional type1 ipRGCs, had already been shown to demonstrate
246 increased survival to mechanical and metabolic stresses[52]. However, the morphological and
247 functional alterations observed in AD donor remaining ipRGCs suggest that type1 ipRGCs
248 probably also degenerate. If confirmed, these results would suggest that some ipRGC-dependent
249 responses to light may be impacted earlier than others and could constitute stage-specific markers.
250 Overall, these alterations are consistent with and could contribute to the alterations of ipRGC-
251 regulated functions, such as circadian rhythm, sleep/alertness, and mood, experienced by AD
252 patients. Interestingly, large-scale population studies, such as those from the UK Biobank, provide
253 indirect support to our results by reporting associations between light signaling, sleep, and
254 neurodegenerative outcomes[53–55].

255 As PLR is thought to rely on both M1 and M2 ipRGCs[56], our results predict that pupillary
256 responses to light should also be affected. Pupillometry is a scalable, cost effective, non-invasive
257 assay that could easily be used in clinical settings. A few groups have started to explore as a

258 biomarker of AD in pre-symptomatic cases[57,58] and early AD cases[59,60]. However, the results have
259 been mixed. This may reflect the diversity of light stimuli and protocols[61,62] and emphasizes the
260 need to determine the spectral, intensity, and/or temporal domains where ipRGCs malfunction and
261 PLR is impacted. For example, our results suggest that injured ipRGCs will fail to sustain
262 responses to long stimulations at high irradiance.

263 The retina, an extension of the central nervous system, offers a unique opportunity to study
264 AD pathology outside of the brain. Over the past decades, accumulating evidence has shed light
265 on the presence of AD-related histological changes in the retina, suggesting the potential of
266 different retinal imaging modalities as a non-invasive method to detect and study the disease (for
267 review see[34]). Our results suggest that the retinal functions (light perception and transmission to
268 the brain) are also altered and add ipRGC-dependent responses to light as potential biomarkers of
269 AD. In AD donors, surviving ipRGCs seem to recapitulate several phenotypes observed in brain
270 neurons: hyperexcitability and ballooning. This, together with the fact that they are more accessible
271 and have clear cellular and behavioral readouts, makes ipRGCs a promising model to study the
272 mechanisms of neuronal degeneration directly in humans. Elucidating the mechanisms underlying
273 ipRGC vulnerability to AD could lead to the discovery of therapeutic targets to improve patients'
274 quality of life and potentially improve the overall disease trajectory.

275

276 **Limitations**

277 Our study has a number of limitations. First, our sample size is small because of the
278 challenges presented in obtaining and collecting postmortem eye and brain tissues from well-
279 characterized participants meeting the criteria of inclusion. However, we partially compensated
280 for this limitation by using in-depth objective physiopathological and functional measurements

281 from each donor. Secondly, our cohort has a greater proportion of male subjects, leading to
282 potential sex-related bias. Our study population was composed primarily of self-reported White
283 and thus may not be representative of other populations. Third, because our focus was on
284 physiology, the pieces of retina were collected in the same central region, irrespective of the
285 orientation. While this strategy may have caused some variability as ipRGC density varies between
286 people[28], ipRGC density and distribution is relatively homogenous in this region within subject[25].
287 It may also have left apart more important alterations in the peripheral retina[17,29,63,64]. Finally, our
288 study is primarily correlational and, therefore, caution must be taken before making cause-and-
289 effect inferences.

290 Despite these limitations, the present study provides a first glimpse of the
291 pathophysiological mechanisms of neurodegeneration at work in humans. Quantitative studies in
292 larger cohorts and animal models of AD will be necessary to confirm these results and
293 mechanistically dissect the processes underlying ipRGC vulnerability to AD. This work has the
294 potential to influence both AD research and clinical practice by highlighting the retina as a window
295 into brain pathology.

296

297

298 **Methods**

299 *Donors*

300 The donors were patients of both sexes from the Geneva Stroke Center who had died following a
301 vascular event. Aside from the stroke, they were either cognitively healthy, diagnosed with
302 Alzheimer's disease (AD), or showed signs of neurodegeneration. Patients were prospectively
303 included in the study after obtaining informed consent from family members or legal healthcare
304 proxies. In a second phase, following confirmation of death, the patients were promptly transported
305 to the hospital morgue, where enucleation was performed immediately, day or night, by a trained
306 physician (NS). After collection, the eyes were immediately transferred to the laboratory in a light-
307 proof, thermally insulated container filled with continuously oxygenated Ames' medium, as
308 previously described [22,23]. Only patients for whom enucleation was completed within two hours
309 post-mortem were included in the study (Table1), as photoreceptor function can be reliably
310 recovered and recorded within this time window [22,23].

311

312 *Eye sampling procedure*

313 Bilateral enucleation was performed in all eligible patients following a standard surgical
314 procedure. After insertion of a lid speculum, a conjunctival peritomy was performed using a #15
315 blade, followed by dissection of Tenon's capsule. The extraocular muscles were identified,
316 isolated, and transected, facilitating identification and isolation of the optic nerve from the
317 surrounding structures. Using microscissors, the optic nerve was then sharply transsected, as far
318 as possible from its bulbar insertion to the ocular globe, closest possible to the orbital apex. After
319 being freed from its orbital attachments, the eyeballs were removed from the orbital cavity. A 360-
320 degree concentric limbal incision allowed the removal of cornea, iris, and the lens. Following this

procedure, eyeballs were transported to the laboratory in a custom-designed container under continuous oxygenation as described previously[22,23].

Exclusion criteria were the presence of known significant posterior pole ocular pathology such as age-related macular degeneration, glaucoma, or other retinopathies or optic neuropathies as well as know systemic pathology like diabetes.

Brain histopathology

The tissue blocks were embedded in paraffin and 12 µm-thick adjacent sections were stained with hematoxylin-eosin or with antibodies against tau (AT8; Pierce Biotechnology, Rockford, IL, USA, 1:1,000, that recognizes the Ser202 and Thr205 epitopes) and Aβ (4G8, Signet Laboratories, Dedham, MA, USA, 1:2,000, that recognizes amino acids 18–22 of the Aβ protein). The neuropathological assessment of Alzheimer disease pathological changes was performed following NIA-AA guidelines[65]. The severity of tau--immunoreactive lesions, amyloid deposition and neuritic plaques was determined using the Braak stages, Thal phases, and CERAD classification[20,21,66].

Retina sampling

The vitreous was removed from the eyecup under dim red light. The macula was identified according to its pigmentation and the pattern of blood vessels in the retina. Circular patches (3 mm diameter) of retina were punched out in an annular region comprised within ~2 to 10 mm from the fovea (except in the blind spot) and from both left and right eyes. Given the number of challenges, including punching out adequate patches, vitreous removal, patches adhesion on the MEA, length of dark adaptation periods and protocol, sampling was done indifferently of the quadrant

344 orientation. While orientation difference may be a source of variability, it seemed a reasonable
345 compromise as this region is relatively homogenous regarding ipRGC density.
346 Samples used for histological experiments were taken in the same region at the end of the recording
347 session and immediately drop in 4% paraformaldehyde (PFA).
348
349 *Retina histopathology*
350 Retinas were fixed in 4% PFA at 4°C for 24 hours, followed by paraffin embedding. Sagittal-
351 oriented sections of the posterior segment were sliced at 10µm thickness. These paraffin sections
352 were treated with 70% formic acid (Roth, 5355.1) for 10 minutes at room temperature, followed
353 by antigen retrieval in citrate buffer (pH 6.0, Merck, 100244) at 100 °C for 1 hour. Sections were
354 then incubated in a blocking solution containing 5% normal goat serum (Sigma, D9663) and 0.05%
355 Triton X-100 (Sigma, T9284) in Tris-buffered saline (TBS; Sigma, 94158) at room temperature
356 for 1 hour. Then, sections were incubated overnight at 4 °C with primary antibodies: anti-Amyloid
357 Beta (ABeta x-42, clone 12F4, mouse, Merck, 05-831-I, 1:500) or anti-Tau (AT8, p-tau
358 Ser202/Thr205, mouse, ThermoFisher, MN1020, 1:250), diluted in 2% blocking buffer. Sections
359 were washed with TBS containing 0.05% Triton X-100, followed by incubation with secondary
360 antibodies (anti-mouse Alexa Fluor® 488, ThermoFisher, A11029, 1:1000) and counterstaining
361 of nuclei with 4′,6-diamidino-2-phenylindole (DAPI; Sigma, D9542) for 3 hours at room
362 temperature. Finally, sections were mounted with Inova Mounting Medium (Ruwag Handels AG,
363 508005). Images were acquired at 40x magnification using a scanning laser microscope (Nikon,
364 Eclipse 80i). Three to six distinct sections imaged per donor. Controls were processed using
365 identical protocols while omitting primary antibody to assess non-specific labelling. The outer and
366 inner retinas, including respectively the photoreceptor and outer plexiform layers and the inner

367 nuclear layer, inner plexiform layer and RGCs layer, were manually segmented using Fiji software
368 (NIH). The average intensity of the aggregates fluorescent signal and the thickness of these regions
369 were measured.
370
371 *Melanopsin Immunofluorescence*
372 Immunohistochemistry was performed as described in detail previously[25,67]. The flat-mount pieces
373 of retinas were incubated in 5% normal donkey serum for 20 min to avoid nonspecific staining.
374 The flat-mount was incubated for 3–4 days with melanopsin primary antibody at 4°C. The patches
375 were then washed and incubated with secondary antibodies for 2 to 3hours at room temperature.
376 Control experiments were performed by eliminating the primary antibody, which abolished all
377 specific staining. Experimenters blinded for the donor ID and pathology were asked to count all
378 cells in the pieces of retina and to trace four representative cells in each patches using semi-
379 automated tracing (pluggin SNT in Fiji).
380
381 *Multi-electrode array recordings*
382 Patches of retina were dark incubated in oxygenated Ames solution until recording (at least
383 60min). Retinal patches were mounted on MEA (256 electrodes arranged in a 16 × 16 square grid,
384 Multichannel Systems, Reutlingen, Germany), ganglion cell side contacting the electrodes, and
385 perfused with oxygenated Ames' medium (Sigma-Aldrich, A1420-10X1L) at 34°C. The
386 MEA2100 amplifier was enclosed in a lightproof box located in a room kept in dark with light
387 emitted only from the controller computer screen with red filter on the screen. ipRGC recordings
388 were done in presence of synaptic blockers (CNQX 20µM, L-AP4 20µM, and D-AP5 50µM) and
389 9-cis retinaldehyde. Stock solutions of 9-cis-Retinal (R5754; Sigma–Aldrich) in ethanol (100 mM)

390 were prepared in darkness and stored at −80°C. On the day of the experiment, an aliquot was
391 thawed and diluted to a final concentration of 100 µM in Ames' medium.
392 Data collection, and analysis were performed as previously described[16,22,68]. Briefly, the signal was
393 acquired at 10 kHz and filtered using a low pass (<500Hz) and a high pass (>300Hz) filters for the
394 mERGs and for the RGC multiunit spike responses respectively. Thresholds for spike detection
395 were set at 5 times the standard deviation of the noise on each channel. Spike cutouts, consisting
396 of 1 msec preceding and 2 msec after a suprathreshold event, along were sorted into trains of a
397 single cell after recording using Offline Sorter (Plexon, Denton, TX). Data analysis and display
398 were performed using Neuroexplorer (Plexon) and custom software written in MATLAB.
399
400 *Light stimulations*
401 To elicit the mERGs, we used sequences of five 10ms monochromatic light pulses (470nm)
402 separated by 10s of darkness at four increasing irradiances (6.10^9, 7.10^{10}, 2.10^{12}, and 2.10^{13}
403 photons/cm^2/s). To generate ipRGC responses, we applied a protocol consisting in a sequence of
404 four 30s light stimulations of increasing irradiance of light (7.10^{10}, 2.10^{12}, 2.10^{13}, 1.10^{14}, and 1.10^{15}
405 photons/cm^2/s at 470nm,) separated by 2min of darkness. All light stimuli were generated by high
406 brightness LED, LuxeonStar 5 located ~20cm at the vertical above the MEA. Stimuli were
407 controlled by a homemade C+ program and synchronized to the electrophysiological recordings.
408 The light intensities were measured with a powermeter (PM120D, Thor labs).
409
410 *ipRGC response parameters analysis*
411 The response discharge rate was calculated as the average of the discharge rate measured during
412 the stimulation (30s) minus the average discharge rate measure during the 30s prior to the

413 stimulation (baseline). The response latency was defined as the delay between the start of the
414 stimulation and the response crossing a threshold set at baseline +2*SD. The response was
415 considered over after firing rate dropped below the baseline level for more than 3 seconds. The
416 dose-response curves (DRCs) were obtained by plotting the response (Y, discharge rate) as a
417 function of the irradiance of the stimulation (X, photon/cm^2/s). DRCs were fitted by a Michaelis-
418 Menten function of the form; Y=Rmax*X/(EC50+X) where Rmax is the maximum response and
419 EC50 is the irradiance required to drive a 50 percent response. A few inhibitory responses were
420 manually discarded.
421
422 *ipRGCs clustering*
423 To distinguish functional types of ipRGCs, we performed principal component analysis (PCA) on
424 sensitivity, duration, and latency of the response as previously described[22,69,70]. PCA allowed
425 reducing the dimensionality of the data set; the first two principal components accounted for
426 almost 65.5% of the variance (PC1=47.1% and PC2=18.4%). Thus, we next performed k-means
427 clustering analysis on the first two principal components. This model produced clusters that
428 corresponded to the initial analysis. To determine the number of ipRGC clusters, the first two
429 principal components were fitted with Gaussian mixture models (GMMs). We produced separate
430 GMMs for 1 to 5 ipRGCs clusters and then used the Akaike information criterion (AIC) to
431 determine which GMM reported best the ipRGCs distribution. When we compared the 1 to 5
432 cluster models, the models with the smallest AIC value (best model) were the 3, 4, and 5 clusters
433 model (AIC values for models at 1 to 5 clusters: 480.3, 386.9, 272.2, 257.5, 240.5, and 238,7
434 respectively). Given the limited number of cells and given the clear inflexion in AIC value at 3,

435 we represented the 3 clusters model as the minimum number of functional subtypes, comparable
436 to previous study[22].
437
438 *Statistics*
439 All data are expressed as means ± SEM unless stated otherwise. GraphPad Prism was used for all
440 statistical analyses. Statistical tests used are stated in the figure's legends. Differences between
441 groups were considered statistically significant for $p<0.05$. Bivariate correlation analysis between
442 histological (ipRGC/mRGC density, Thal/Braak scores, severity of brain pathology) and clinical
443 data (age, collection delay) was performed using Spearman coefficient. Matlab (2019a) was used
444 for k-means and hierarchical clustering, PCA, GMM, and AIC analysis (Statistics and Machine
445 Learning Toolbox). Because of repeated measures on multiples pieces of retina per donor in some
446 experiments, to assess the impact of the disease on measured parameters, we fitted a linear mixed-
447 effects model (LMM) using MATLAB (fitlme). The model included disease as a fixed effect and
448 random intercepts for donor and piece according to the formula: parameter ~ disease (AD vs ND
449 or Thal/Braak score) + (1 | donor) + (1 | piece). Model parameters were estimated by maximum
450 likelihood (ML). Significance of fixed effects was assessed using F-tests with Satterthwaite
451 approximation for degrees of freedom. F and p-values or slope (β) +/- standard error (SE) and p-
452 values given in the respective figure legends.
453
454 *Study approval*
455 Informed consent was obtained either from patients or from family members or legal healthcare
456 proxies in accordance with the protocol approval obtained from the Ethics Cantonal Committee of
457 Geneva (Project 2020-02126).

Data availability

Code and data used to generate the figures described in this paper will be made available via Zenodo (Zenodo.org) at the time of publication, with a DOI to be included here.

Acknowledgements

We thank Christian Dellenbach and Christian Kaiser for the light stimulation device and software, Dr. G. Benegiamo for critical comments on the manuscript, and the Donors and their families. This study was supported by the Velux Stiftung grant to SK and LSM, the Novartis Biomedical Research Foundation grant to LSM, and the Chan Zuckerberg Initiative grant to AA and LSM. JH is supported from the Danish Center for Cellular Communication.

Contributions

NS, DM, and LSM conceptualized the study. NS and LSM designed it. NS coordinated tissue collections and harvests. NS, EK, YT, TAZ, KLE, and LSM performed the experiments. JH provided the melanopsin antibodies. EK, JH, JAL, EC, GT, SK, and AA provided scientific expertise and critical reading of the manuscript. LSM analyzed the data. LSM wrote the first draft, all authors edited and approved the manuscript.

Competing interests

The authors declare that they have no conflict of interests.

Funding

481 This study was supported by the Velux Stiftung grant to SK and LSM, the Novartis Biomedical
482 Research Foundation grant to LSM, and the Chan Zuckerberg Initiative grant to AA and LSM. JH
483 is supported from the Danish Center for Cellular Communication.
484

485 **References**

486 1. Scheltens, P. *et al.* Alzheimer's disease. *The Lancet* **388**, 505–517 (2016).

487 2. Nichols, E. *et al.* Estimation of the global prevalence of dementia in 2019 and forecasted prevalence in
488 2050: an analysis for the Global Burden of Disease Study 2019. *The Lancet Public Health* **7**, e105–
489 e125 (2022).

490 3. Weldemichael, D. A. & Grossberg, G. T. Circadian Rhythm Disturbances in Patients with Alzheimer's
491 Disease: A Review. *International Journal of Alzheimer’s Disease* **2010**, e716453 (2010).

492 4. van Someren, E. J. *et al.* Circadian rest-activity rhythm disturbances in Alzheimer's disease. *Biol*
493 *Psychiatry* **40**, 259–270 (1996).

494 5. Wu, Y.-H. & Swaab, D. F. Disturbance and strategies for reactivation of the circadian rhythm system
495 in aging and Alzheimer's disease. *Sleep Medicine* **8**, 623–636 (2007).

496 6. Uddin, M. S. *et al.* Circadian and sleep dysfunction in Alzheimer's disease. *Ageing Res Rev* **60**, 101046
497 (2020).

498 7. Videnovic, A., Lazar, A. S., Barker, R. A. & Overeem, S. 'The clocks that time us'--circadian rhythms
499 in neurodegenerative disorders. *Nat Rev Neurol* **10**, 683–693 (2014).

500 8. Musiek, E. S. *et al.* Circadian Rest-Activity Pattern Changes in Aging and Preclinical Alzheimer
501 Disease. *JAMA Neurol* https://doi.org/10.1001/jamaneurol.2017.4719 (2018)
502 doi:10.1001/jamaneurol.2017.4719.

503 9. Tsapanou, A. *et al.* Daytime Sleepiness and Sleep Inadequacy as Risk Factors for Dementia. *DEE* **5**,
504 286–295 (2015).

505 10. Hahn, E. A., Wang, H.-X., Andel, R. & Fratiglioni, L. A Change in Sleep Pattern May Predict
506 Alzheimer Disease. *The American Journal of Geriatric Psychiatry* **22**, 1262–1271 (2014).

507 11. Sterniczuk, R., Theou, O., Rusak, B. & Rockwood, K. Sleep Disturbance is Associated with Incident
508 Dementia and Mortality. *Current Alzheimer Research* **10**, 767–775.

509 12. Musiek, E. S., Xiong, D. D. & Holtzman, D. M. Sleep, circadian rhythms, and the pathogenesis of
510 Alzheimer Disease. *Exp Mol Med* **47**, e148 (2015).

511 13. Güler, A. D. *et al.* Melanopsin cells are the principal conduits for rod-cone input to non-image-forming
512 vision. *Nature* **453**, 102–105 (2008).
513 14. Hatori, M. *et al.* Inducible ablation of melanopsin-expressing retinal ganglion cells reveals their central
514 role in non-image forming visual responses. *PLoS ONE* **3**, e2451 (2008).
515 15. Altimus, C. M. *et al.* Rods-cones and melanopsin detect light and dark to modulate sleep independent
516 of image formation. *Proc. Natl. Acad. Sci. U.S.A* **105**, 19998–20003 (2008).
517 16. Mure, L. S. *et al.* Melanopsin-Encoded Response Properties of Intrinsically Photosensitive Retinal
518 Ganglion Cells. *Neuron* **90**, 1016–1027 (2016).
519 17. Morgia, C. L. *et al.* Melanopsin retinal ganglion cell loss in Alzheimer disease. *Annals of Neurology*
520 **79**, 90–109 (2016).
521 18. Carrero, L. *et al.* Disturbed circadian rhythm and retinal degeneration in a mouse model of Alzheimer's
522 disease. *Acta Neuropathologica Communications* **11**, 55 (2023).
523 19. Weigel, T. K., Guo, C. L., Güler, A. D. & Ferris, H. A. Altered circadian behavior and light sensing in
524 mouse models of Alzheimer's disease. *Frontiers in Aging Neuroscience* **15**, (2023).
525 20. Braak, H. & Braak, E. Neuropathological stageing of Alzheimer-related changes. *Acta Neuropathol*
526 **82**, 239–259 (1991).
527 21. Thal, D. R., Rüb, U., Orantes, M. & Braak, H. Phases of A beta-deposition in the human brain and its
528 relevance for the development of AD. *Neurology* **58**, 1791–1800 (2002).
529 22. Mure, L. S., Vinberg, F., Hanneken, A. & Panda, S. Functional diversity of human intrinsically
530 photosensitive retinal ganglion cells. *Science* **366**, 1251–1255 (2019).
531 23. Abbas, F. *et al.* Revival of light signalling in the postmortem mouse and human retina. *Nature* 1–7
532 (2022) doi:10.1038/s41586-022-04709-x.
533 24. Fujii, M., Sunagawa, G. A., Kondo, M., Takahashi, M. & Mandai, M. Evaluation of micro
534 Electroretinograms Recorded with Multiple Electrode Array to Assess Focal Retinal Function. *Sci Rep*
535 **6**, 30719 (2016).

536 25. Hannibal, J., Christiansen, A. T., Heegaard, S., Fahrenkrug, J. & Kiilgaard, J. F. Melanopsin expressing
537 human retinal ganglion cells: Subtypes, distribution, and intraretinal connectivity. *Journal of*
538 *Comparative Neurology* **525**, 1934–1961 (2017).
539 26. Liao, H.-W. *et al.* Melanopsin-expressing ganglion cells on macaque and human retinas form two
540 morphologically distinct populations. *J. Comp. Neurol.* **524**, 2845–2872 (2016).
541 27. Esquiva, G., Lax, P., Pérez-Santonja, J. J., García-Fernández, J. M. & Cuenca, N. Loss of Melanopsin-
542 Expressing Ganglion Cell Subtypes and Dendritic Degeneration in the Aging Human Retina. *Front*
543 *Aging Neurosci* **9**, (2017).
544 28. Nasir-Ahmad, S., Lee, S. C. S., Martin, P. R. & Grünert, U. Melanopsin-expressing ganglion cells in
545 human retina: Morphology, distribution, and synaptic connections. *J. Comp. Neurol.*
546 https://doi.org/10.1002/cne.24176 (2017) doi:10.1002/cne.24176.
547 29. Hart de Ruyter, F. J. *et al.* Phosphorylated tau in the retina correlates with tau pathology in the brain in
548 Alzheimer's disease and primary tauopathies. *Acta Neuropathol* **145**, 197–218 (2023).
549 30. Schön, C. *et al.* Long-term in vivo imaging of fibrillar tau in the retina of P301S transgenic mice. *PLoS*
550 *One* **7**, e53547 (2012).
551 31. Koronyo-Hamaoui, M. *et al.* Identification of amyloid plaques in retinas from Alzheimer's patients and
552 noninvasive in vivo optical imaging of retinal plaques in a mouse model. *NeuroImage* **54**, S204–S217
553 (2011).
554 32. Koronyo, Y. *et al.* Retinal pathological features and proteome signatures of Alzheimer's disease. *Acta*
555 *Neuropathol* **145**, 409–438 (2023).
556 33. La Morgia, C. *et al.* Multimodal investigation of melanopsin retinal ganglion cells in Alzheimer's
557 disease. *Annals of Clinical and Translational Neurology* **n/a**, (2023).
558 34. Mirzaei, N. *et al.* Alzheimer's Retinopathy: Seeing Disease in the Eyes. *Front. Neurosci.* **14**, (2020).
559 35. Cronin-Golomb, A., Sugiura, R., Corkin, S. & Growdon, J. H. Incomplete achromatopsia in
560 Alzheimer's disease. *Neurobiol Aging* **14**, 471–477 (1993).

561 36. Schlotterer, G., Moscovitch, M. & Crapper-McLachlan, D. Visual processing deficits as assessed by
562 spatial frequency contrast sensitivity and backward masking in normal ageing and Alzheimer's disease.
563 *Brain* **107 (Pt 1)**, 309–325 (1984).
564 37. Sadun, A. A., Borchert, M., DeVita, E., Hinton, D. R. & Bassi, C. J. Assessment of visual impairment
565 in patients with Alzheimer's disease. *Am J Ophthalmol* **104**, 113–120 (1987).
566 38. Trick, G. L., Trick, L. R., Morris, P. & Wolf, M. Visual field loss in senile dementia of the Alzheimer's
567 type. *Neurology* **45**, 68–74 (1995).
568 39. Katz, B. & Rimmer, S. Ophthalmologic manifestations of Alzheimer's disease. *Surv Ophthalmol* **34**,
569 31–43 (1989).
570 40. Trick, G. L., Barris, M. C. & Bickler-Bluth, M. Abnormal pattern electroretinograms in patients with
571 senile dementia of the Alzheimer type. *Ann Neurol* **26**, 226–231 (1989).
572 41. Parisi, V. *et al.* Morphological and functional retinal impairment in Alzheimer's disease patients. *Clin*
573 *Neurophysiol* **112**, 1860–1867 (2001).
574 42. Sartucci, F. *et al.* Dysfunction of the magnocellular stream in Alzheimer's disease evaluated by pattern
575 electroretinograms and visual evoked potentials. *Brain Res Bull* **82**, 169–176 (2010).
576 43. Krasodomska, K., Lubiński, W., Potemkowski, A. & Honczarenko, K. Pattern electroretinogram
577 (PERG) and pattern visual evoked potential (PVEP) in the early stages of Alzheimer's disease. *Doc*
578 *Ophthalmol* **121**, 111–121 (2010).
579 44. Hattar, S. *et al.* Central projections of melanopsin-expressing retinal ganglion cells in the mouse. *J.*
580 *Comp. Neurol* **497**, 326–349 (2006).
581 45. Beier, C., Zhang, Z., Yurgel, M. & Hattar, S. Projections of ipRGCs and conventional RGCs to
582 retinorecipient brain nuclei. *J Comp Neurol* https://doi.org/10.1002/cne.25061 (2020)
583 doi:10.1002/cne.25061.
584 46. Cobos, I. & Palop, J. J. Swollen axons impair neuronal circuits in Alzheimer's disease. *Nature* **612**,
585 218–220 (2022).

586 47. Michaud, J. *et al.* Ballooned neurons in semi-recent severe traumatic brain injury. *Acta*
587 *Neuropathologica Communications* **11**, 37 (2023).
588 48. Lowe, J. *et al.* Ballooned neurons in several neurodegenerative diseases and stroke contain αB
589 crystallin. *Neuropathology and Applied Neurobiology* **18**, 341–350 (1992).
590 49. Bassett, S. S. *et al.* Familial risk for Alzheimer's disease alters fMRI activation patterns. *Brain* **129**,
591 1229–1239 (2006).
592 50. Filippini, N. *et al.* Distinct patterns of brain activity in young carriers of the *APOE*-ε4 allele.
593 *Proceedings of the National Academy of Sciences* **106**, 7209–7214 (2009).
594 51. Targa Dias Anastacio, H., Matosin, N. & Ooi, L. Neuronal hyperexcitability in Alzheimer's disease:
595 what are the drivers behind this aberrant phenotype? *Transl Psychiatry* **12**, 1–14 (2022).
596 52. Cui, Q., Ren, C., Sollars, P. J., Pickard, G. E. & So, K.-F. THE INJURY RESISTANT ABILITY OF
597 MELANOPSIN-EXPRESSING INTRINSICALLY PHOTOSENSITIVE RETINAL GANGLION
598 CELLS. *Neuroscience* **284**, 845–853 (2015).
599 53. Ma, L.-Z. *et al.* Time spent in outdoor light is associated with the risk of dementia: a prospective cohort
600 study of 362094 participants. *BMC Med* **20**, 132 (2022).
601 54. Burns, A. C. *et al.* Time spent in outdoor light is associated with mood, sleep, and circadian rhythm-
602 related outcomes: A cross-sectional and longitudinal study in over 400,000 UK Biobank participants.
603 *J Affect Disord* **295**, 347–352 (2021).
604 55. Milligan Armstrong, A. *et al.* Exploring the relationship between melanopsin gene variants, sleep, and
605 markers of brain health. *Alzheimer's & Dementia: Diagnosis, Assessment & Disease Monitoring* **17**,
606 e70056 (2025).
607 56. Baver, S. B., Pickard, G. E., Sollars, P. J. & Pickard, G. E. Two types of melanopsin retinal ganglion
608 cell differentially innervate the hypothalamic suprachiasmatic nucleus and the olivary pretectal
609 nucleus. *Eur. J. Neurosci.* **27**, 1763–1770 (2008).
610 57. Oh, A. J. *et al.* Pupillometry evaluation of melanopsin retinal ganglion cell function and sleep-wake
611 activity in pre-symptomatic Alzheimer's disease. *PLoS ONE* **14**, e0226197 (2019).

612 58. Van Stavern, G. P., Bei, L., Shui, Y.-B., Huecker, J. & Gordon, M. Pupillary light reaction in preclinical
613 Alzheimer's disease subjects compared with normal ageing controls. *Br J Ophthalmol* **103**, 971–975
614 (2019).
615 59. Kawasaki, A., Ouanes, S., Crippa, S. V. & Popp, J. Early-Stage Alzheimer's Disease Does Not Alter
616 Pupil Responses to Colored Light Stimuli. *J. Alzheimers Dis.* **75**, 1273–1282 (2020).
617 60. Romagnoli, M. *et al.* Chromatic Pupillometry Findings in Alzheimer's Disease. *Front. Neurosci.* **14**,
618 (2020).
619 61. Chougule, P. S., Najjar, R. P., Finkelstein, M. T., Kandiah, N. & Milea, D. Light-Induced Pupillary
620 Responses in Alzheimer's Disease. *Front Neurol* **10**, 360 (2019).
621 62. Romagnoli, M., Amore, G., Avanzini, P., Carelli, V. & La Morgia, C. Chromatic pupillometry for
622 evaluating melanopsin retinal ganglion cell function in Alzheimer's disease and other
623 neurodegenerative disorders: a review. *Front Psychol* **14**, 1295129 (2023).
624 63. den Haan, J. *et al.* Amyloid-beta and phosphorylated tau in post-mortem Alzheimer's disease retinas.
625 *Acta Neuropathologica Communications* **6**, 147 (2018).
626 64. Koronyo, Y. *et al.* Retinal amyloid pathology and proof-of-concept imaging trial in Alzheimer's
627 disease. *JCI Insight* **2**, e93621, 93621 (2017).
628 65. Hyman, B. T. *et al.* National Institute on Aging-Alzheimer's Association guidelines for the
629 neuropathologic assessment of Alzheimer's disease. *Alzheimers Dement* **8**, 1–13 (2012).
630 66. Mirra, S. S. *et al.* The Consortium to Establish a Registry for Alzheimer's Disease (CERAD). Part II.
631 Standardization of the neuropathologic assessment of Alzheimer's disease. *Neurology* **41**, 479–486
632 (1991).
633 67. Hannibal, J. *et al.* Central projections of intrinsically photosensitive retinal ganglion cells in the
634 macaque monkey. *J. Comp. Neurol.* **522**, 2231–2248 (2014).
635 68. Mure, L. S. *et al.* Sustained Melanopsin Photoresponse Is Supported by Specific Roles of β-Arrestin 1
636 and 2 in Deactivation and Regeneration of Photopigment. *Cell Reports* **25**, 2497-2509.e4 (2018).

637 69. Emanuel, A. J., Kapur, K. & Do, M. T. H. Biophysical Variation within the M1 Type of Ganglion Cell
638 Photoreceptor. *Cell Rep* **21**, 1048–1062 (2017).
639 70. Tu, D. C. *et al.* Physiologic diversity and development of intrinsically photosensitive retinal ganglion
640 cells. *Neuron* **48**, 987–999 (2005).
641
642

Table1: Donor's demographic and pathology. Amyloid and tau pathologies were evaluated with Thal phases and Braak stages respectively.

	Age (years)	*Sex*	*Delay to Brain collection (hours)*	*Delay to Eyes collection (hours)*	*Cause of death*	*Thal βAmyloid (A)*	*Braak NFT (B)*	*CERAD (C)*	*CAA*	*Brain histology*	*Retina histology*	*Retina function*	*Figure symbols*
D1	71	M	6	2	Brain infarct, hemorrhage	0 (0)	II (1)	0	+	X	x	x	●
D2	80	F	25	2	Brain infarct	2 (1)	III (2)	2	-	X	x	x	■
D3	77	M	13	2	Brain hemorrhage	4 (3)	VI (3)	3	+	X	x	x	▲
D4	85	M	34	2	Brain hemorrhage	2 (3)	I (1)	0	+	X			
D5	89	F	114	1.5	Brain infarct	3 (2)	V (3)	2	+	X	x	x	▼
D6	97	M	27	9	Brain infarct	4 (3)	II (1)	0	+	X			
D7	103	F	3	1	Brain infarct	1 (1)	II (1)	0	-	X			
D8	74	M	11	0.5	Brain infarct	1 (1)	II (1)	0	-	X	x	x	○
D9	74	M	46	2	Brain infarct	0 (0)	I (1)	0	-	X			
D10	70	F	82	82	Brain hemorrhage	0 (0)	II (1)	0	-	X			
D11	77	M	41	2	Brain hemorrhage	2(1)	II (1)	0	-	X	x		♦
D12	69	M	20	2	Brain infarct	0 (0)	I (1)	0	-	X			
D13	91	M	18	2	Brain hemorrhage	2 (1)	0 (0)	0	-	X	x	x	□

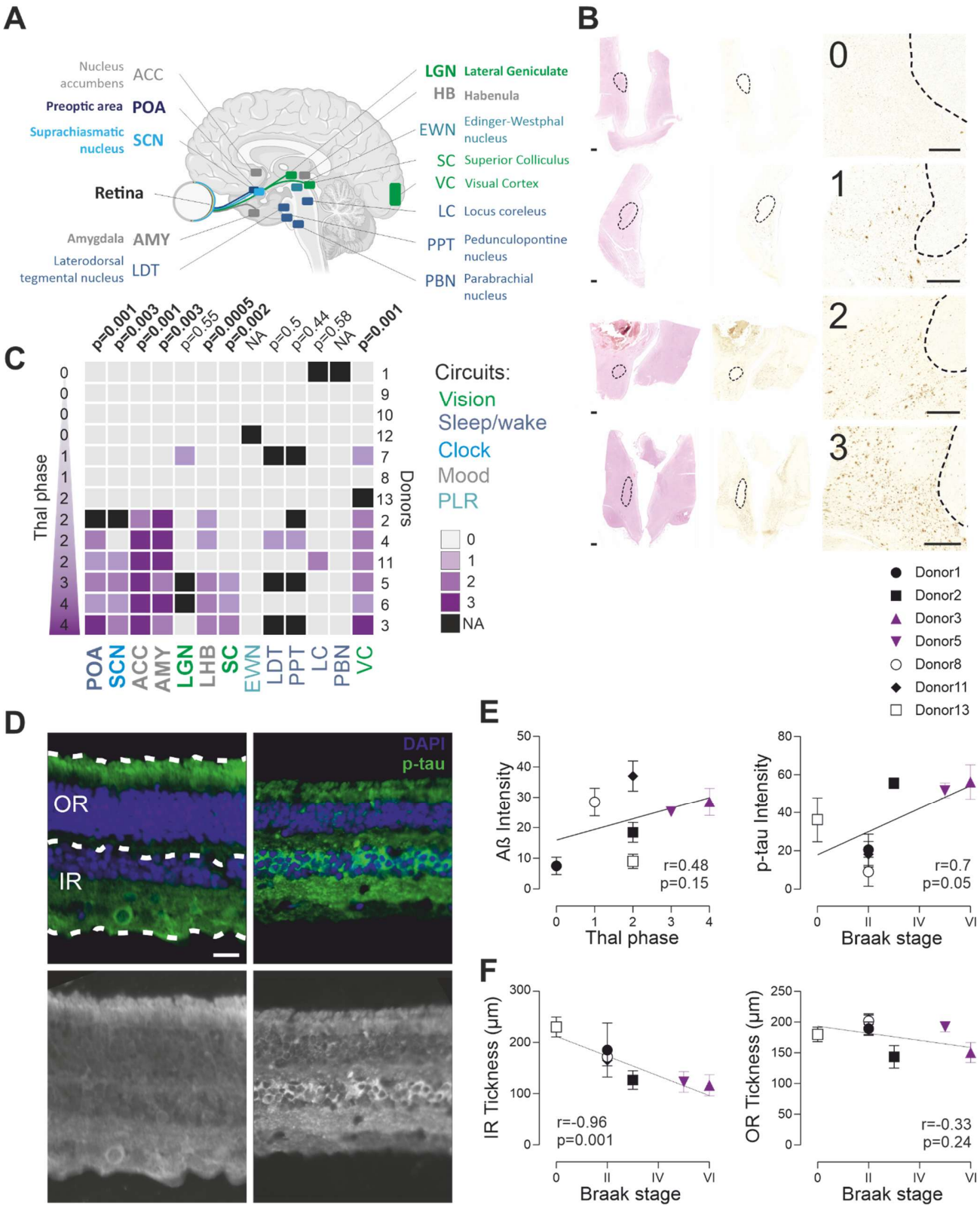
A
Nucleus accumbens ACC
Preoptic area POA
Suprachiasmatic nucleus SCN
Retina
Amygdala AMY
Laterodorsal tegmental nucleus LDT
LGN Lateral Geniculate
HB Habenula
EWN Edinger-Westphal nucleus
SC Superior Colliculus
VC Visual Cortex
LC Locus coreleus
PPT Pedunculopontine nucleus
PBN Parabrachial nucleus
B
0
1
2
3
Donor1
Donor2
Donor3
Donor5
Donor8
Donor11
Donor13
C
p=0.001 p=0.003 p=0.001 p=0.003 p=0.55 p=0.0005 p=0.002 NA p=0.5 p=0.44 p=0.58 NA p=0.001
Thal phase
Donors
Circuits:
Vision
Sleep/wake
Clock
Mood
PLR
0
1
2
3
NA
POA SCN ACC AMY LGN LHB SC EWN LDT PPT LC PBN VC
D
OR
IR
DAPI
p-tau
E
Aß Intensity
Thal phase
r=0.48
p=0.15
p-tau Intensity
Braak stage
r=0.7
p=0.05
F
IR Tickness (µm)
Braak stage
r=-0.96
p=0.001
OR Tickness (µm)
Braak stage
r=-0.33
p=0.24

648

Figure 1: AD hallmarks are present along the circuit of light perception. (**A**) Several brain nuclei contributing to the main light-regulated function (vision, entrainment of the circadian clock, PLR, sleep/alertness, mood) were collected. (**B**) Hypothalamic region including POA from 4 donors exhibiting increasing levels of Aβ deposits (scored 0 to 3). *Left, middle, and right columns,* H&E staining, Aβ staining, and related enlargement respectively (*dotted lines*, fornix; scale bars, 1mm). (**C**) Aβ deposits scores for each brain nuclei in each donor ranked as a function of their Thal phase. (**D**) Fluorescence micrographs of retinal cross-sections from donor 7 (ND, left column) and donor 3 (AD, right column) with Thal phases 2 and 5 and Braak scores II and VI respectively. On the upper left panel, dotted lines materialized the definition of the Outer and Inner retinas (OR and IR). (*Upper row*) Tissues were immunolabeled for p-tau (AT8, green), and DAPI+-nuclei (blue;). Scale bar: 50 µm. (*Lower row*) Greyscale micrographs the same individuals immunolabeled with p-tau (Scale bar: 50 µm). Scatter plots of the thickness of the donors' IR (**E**) and OR (**F**) as a function of their Braak score (n= 3 to 9 sections measured, Spearman correlation coefficient and p value). Scatter plots of the Aβ (**G**) and p-tau (**H**) burdens measured in each donors as a function of the Thal phase and Braak scores of the donors respectively (n=3 to 5 for Aβ and n=3 for Tau per donor, Spearman correlation coefficient and p value).

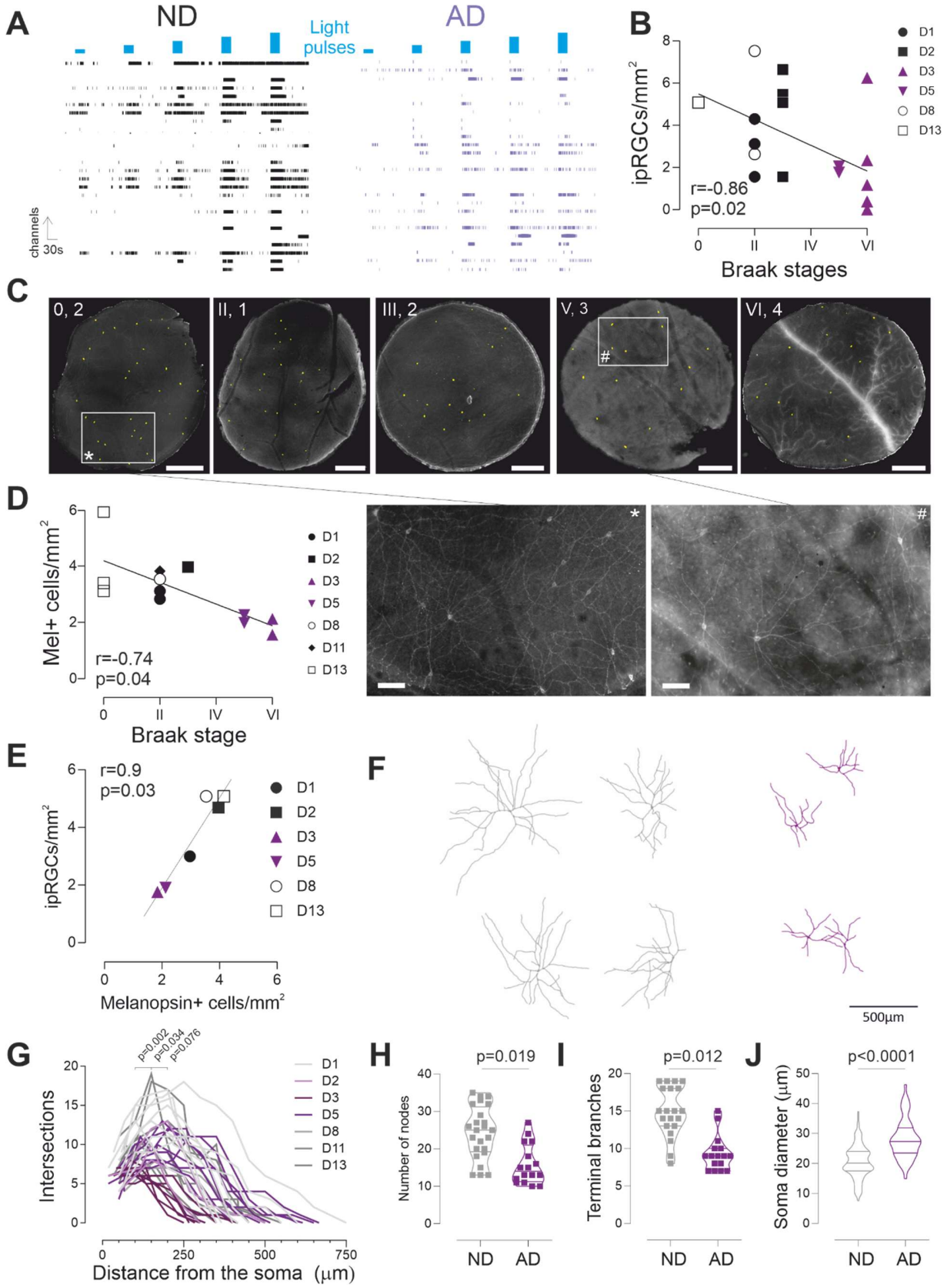
A
ND
Light pulses
AD
channels
30s
B
ipRGCs/mm²
r=-0.86
p=0.02
Braak stages
D1
D2
D3
D5
D8
D13
C
0, 2
II, 1
III, 2
V, 3
VI, 4
D
Mel+ cells/mm²
r=-0.74
p=0.04
Braak stage
D11
E
ipRGCs/mm²
r=0.9
p=0.03
Melanopsin+ cells/mm²
F
500µm
G
Intersections
p=0.002
p=0.034
p=0.076
Distance from the soma (µm)
H
Number of nodes
p=0.019
ND
AD
I
Terminal branches
p=0.012
J
Soma diameter (µm)
p<0.0001

666

Figure 2: ipRGCs decline in AD. (A) Representative ipRGC spike trains to a 30-s light pulses of increasing irradiance (~10^{10} to 10^{15} photons/cm^2/s, 470 nm) from AD and age-matched ND donors. (**B**) ipRGCs density in pieces of retina from each donor as a function of their Braak score (n=1 to 5 retina pieces per donor). (**C**, *Upper row*) Microphotographs of patches of retina immunostained against melanopsin (scale bar 500µm, *upper right corner*, Braak stage and Thal phase of the donors). (*Lower row*) Enlargements from the first (*) and fourth (#) patch microphotographs (scale bar 100µm). The mel+ cells density in each donor correlates with their Braak score (**D**, n=1 to 2 retina pieces per donor) and with the density of ipRGCs reported in the same donors (Spearman correlation, **E**). (**F**) Examples of dendritic shrinkage, mel+ cells from AD (Donor3, *purple*) and age-matched (Donor1, *grey*) donors (scale bar 500µm). (**G**) Scholl analysis (Linear Mixed-effect model (LMM), interaction $F(14,555)=3.7263$, $p<0.001$, FDR-corrected post hoc contrast p-values on the figure), (**H**) number of nodes, (**I**) number of terminal branches, and (**J**) soma diameter from AD (n=8 cells per donor, 2 donors, *purple*) and age-matched (n= 4 to 8 cells per donor, 4 donors, *grey*) donors were different (LMM, $F(1,38)=5.99$ and $F(1,38)=6.98$, H and I respectively, $F(1,199)=36.522$, J).

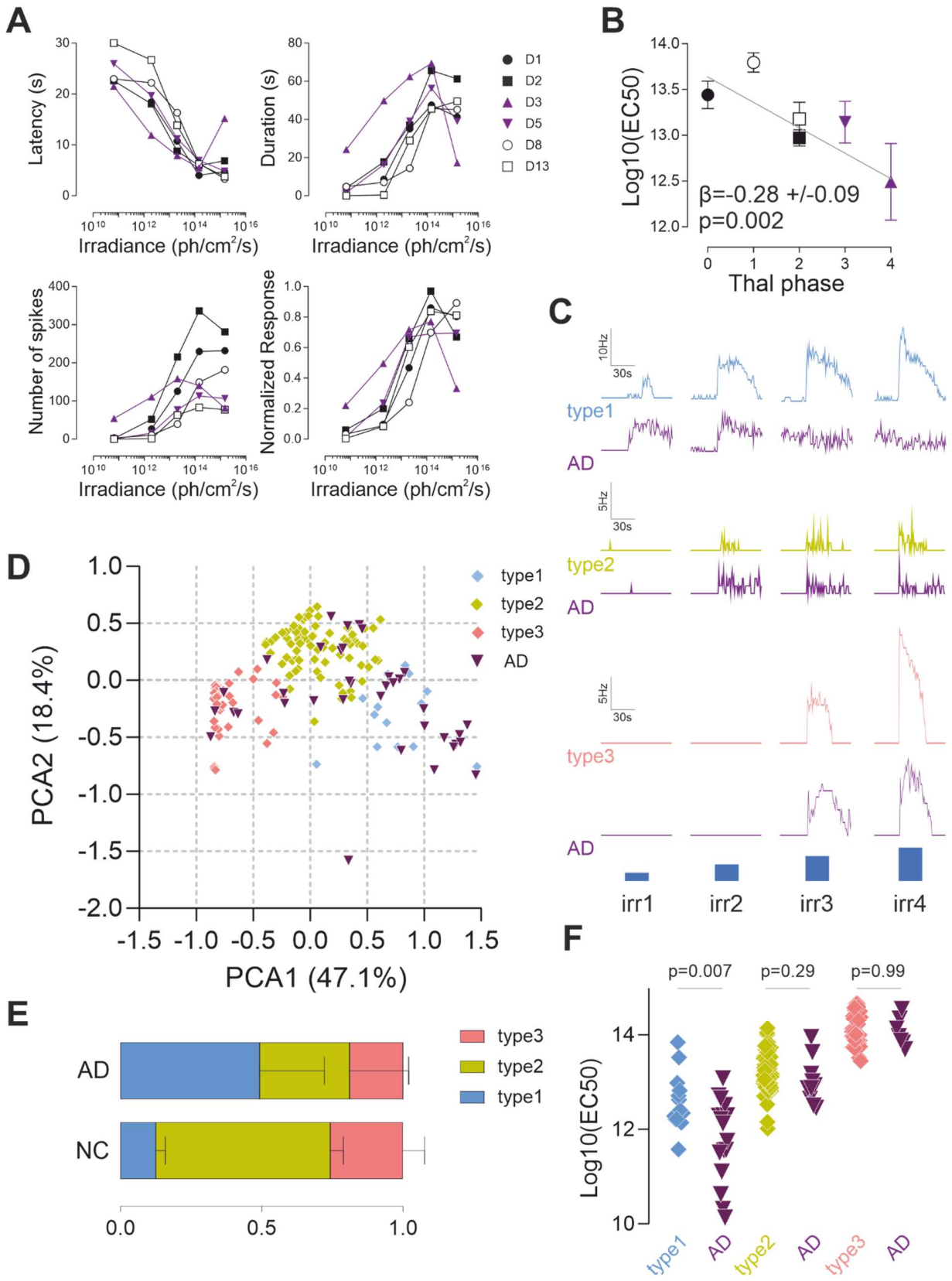
A
Latency (s)
Duration (s)
Number of spikes
Normalized Response
Irradiance (ph/cm²/s)
D1
D2
D3
D5
D8
D13
B
Log10(EC50)
β=-0.28 +/-0.09
p=0.002
Thal phase
C
10Hz
30s
5Hz
type1
type2
type3
AD
irr1
irr2
irr3
irr4
D
PCA2 (18.4%)
PCA1 (47.1%)
type1
type2
type3
AD
E
AD
NC
type3
type2
type1
F
p=0.007
p=0.29
p=0.99
Log10(EC50)
type1
AD
type2
AD
type3
AD

683

684 **Figure 3: ipRGC function is altered in AD.** (**A**) Average ipRGCs'response latency, duration,
685 number of spikes, and normalized response in each donor (n=28, 15, 18, 19, 77, and 13 for donors
686 1, 2, 3, 5, 8, and 13 respectively, where n is the number of cells) to a sequence of 30s light pulses
687 of increasing irradiance (~10^{10} to 10^{15} photons/cm^2/s, 470 nm). (**B**) Average ipRGC sensitivity to
688 light as a function of Thal phase (LMM, slope β +/-SE). (**C**) Representative responses from types
689 1, 2, and 3 ipRGCs to increasing irradiance light pulses (30 s, 470 nm, irradiances (irr) 1, 2, 3, and
690 4: $2x10^{12}$, $2x10^{13}$, $1.5x10^{14}$, and $1.5x10^{15}$ photons/cm^2/s, respectively). Blue bars indicate light
691 pulses. (**D**) Principal components of the ipRGCs' response parameters (sensitivity, latency, and
692 duration; n =133 and n=37, four control and two AD donors (*purple*) respectively). (**E**)
693 Distribution of ipRGC subtypes in ND and AD donors. (**F**) ipRGC sensitivity by subtype in ND
694 and AD donors (n=14, 77, and 45, type1, 2, and 3 cells and n=18, 12, and 7 type1, 2, and 3 cells
695 respectively, LMM F(1,30)=8.43 type 1, F(1,87)=1.09 type 2, F(1,50)= $2.2.10^{-6}$, type 3).